

**Willem-Jan Evers<sup>1</sup>**

Dynamics and Control Group,  
Department of Mechanical Engineering,  
Eindhoven University of Technology,  
Eindhoven 5600 MB, The Netherlands  
e-mail: wjeevers@gmail.com

**Arjan Teerhuis**

e-mail: arjan.teerhuis@tno.nl

**Albert van der Knaap**

Integrated Safety,  
TNO Automotive,  
Helmond 5700 AT, The Netherlands

**Igo Besselink**

e-mail: i.j.m.besselink@tue.nl

**Henk Nijmeijer**

e-mail: h.nijmeijer@tue.nl

Dynamics and Control Group,  
Department of Mechanical Engineering,  
Eindhoven University of Technology,  
Eindhoven 5600 MB, The Netherlands

# The Electromechanical Low-Power Active Suspension: Modeling, Control, and Prototype Testing

*The high energy consumption of market-ready active suspension systems is the limiting factor in the competition with semi-active devices. The variable geometry active suspension is an alternative with a significantly lower power consumption. However, previous designs suffer from packaging problems, nonlinear stiffness characteristics, and failsafe issues. This paper discusses the feasibility of a recently presented, new design, variable geometry actuator, which has a fixed spring and constant stiffness. An actuator model is derived that includes the electric motor and friction characteristics. Using this model, a cascaded controller is developed and the steady-state and dynamic properties are evaluated. The simulation results are validated with prototype tests. The results show a good correspondence between simulations and measurements. Furthermore, a 10 Hz bandwidth can be easily obtained. It is concluded that the electromechanical low-power active suspension design is feasible and that the model gives a fairly accurate representation of both the steady-state and dynamic characteristics of the prototype.*

[DOI: 10.1115/1.4003278]

## 1 Introduction

The main functions of a suspension system are to carry the weight of the suspended mass and to reduce the effect of environmental vibrations, i.e., to limit the transmissibility. This can be achieved with passive elements, such as springs and dampers, but also with (semi) active elements. Herein, semi-active elements have the property that they can only dissipate energy, where active elements can also add energy to the suspension.

Semi-active suspensions typically consist of dampers with a controlled damping constant [1]. This variation can either be achieved mechanically, e.g., by controlling an orifice or using so called “smart fluids” [2]. The latter can be roughly divided into two classes: magnetorheological (MR) and electrorheological (ER) dampers [3]. Semi-active suspensions generally have a low energy consumption (related to electric actuation of valve spools) while still giving improved performance in comparison to passive suspensions. However, in theory, the performance is substantially lower than what is obtainable with active suspensions [4].

The most used active suspension element is probably the air spring [5]. It consumes relatively little energy and typically has a low bandwidth. As such, it is often used for load leveling. Still, in combination with a preview control strategy, these pneumatic suspensions may have more potential [6]. Hydraulic actuators on the other hand can reach far higher bandwidths, see for example Ref. [7]. An example of an active hydraulic suspension (in an automotive context) is the *DaimlerChrysler active body control system* [8], which reaches a bandwidth of approximately 5 Hz. However, hydraulic actuators generally have a relatively high power consumption. One alternative to lower the power consumption is the

use of electromagnetic actuators [9–11] as these have the capability to regenerate energy. Another alternative would be the use of a variable geometry actuator.

The variable geometry actuator was first presented as a 3D concept called the *Delft active suspension* (DAS) [12,13], see Fig. 1. The basic idea behind the concept is based on a wishbone (with length  $l$ ), which can be rotated over an angle  $\alpha$  and is connected to a pretensioned spring at a variable length  $x$ . The spring pretension generates an effective actuator force  $F_{\text{act}}$  at the end of the wishbone (equilibrium of moments). This force can be manipulated by changing the spring position with the motor force  $F_{\text{motor}}$ . The wishbone is connected at one end to the suspended mass—the vehicle chassis in this case—and to the unsuspended mass at the other. Herein, the unsuspended mass—the axle and wheel—is typically subjected to a variable tire force  $F_{\text{tyre}}$ . The effects of this force on both masses can be minimized by choosing a suitable control strategy for  $F_{\text{act}}$  and thus  $x$ . The change of the position  $x$ , the variation of geometry, can be realized with relatively little energy when the spring force is perpendicular to the direction of motion. Consequently, in the idealized case without friction or inertia of the moving spring, any actuator force can be realized without consuming energy.

The Delft active suspension has been built and implemented in a passenger car [14]. Measurements show that the power consumption is significantly lower than that of other known active suspension systems. Under worst-case conditions, with a full sky-hook control implementation, the average power consumption is around 500 W with peaks up to 2.5 kW. Friction and electric losses are assumed to be the main causes. It seems reasonable to assume that the performance could have been further improved if the passive dampers had been optimized. The reported reduction of the root-mean-square accelerations (about 10%) is relatively low and is mainly concentrated around the dominant sprung mass oscillation mode. The subjective ratings of the ride comfort improvement, on the other hand, are much higher. This is mainly the

<sup>1</sup>Corresponding author.

Contributed by the Dynamic Systems Division of ASME for publication in the JOURNAL OF DYNAMIC SYSTEMS, MEASUREMENT, AND CONTROL. Manuscript received January 8, 2010; final manuscript received September 23, 2010; published online April 11, 2011. Assoc. Editor: John R. Wagner.

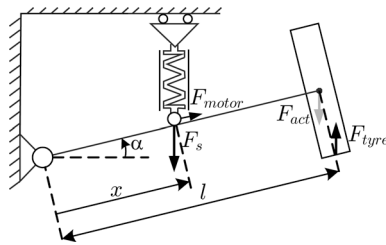


Fig. 1 The DAS [13]

result of the fact that the nonactive system is used as reference. Consequently, the benefit of removing the stiff roll-stabilizer does not show. Furthermore, the additional pitch and roll stability when cornering, braking, or accelerating is not valued in the comfort criterion.

In Ref. [2], it is stated that despite the shortcomings of the practical realization of the Delft Active Suspension “the concept is expected to have significant practical ride improvement potential, which may be materialized through further developments and design changes.” In Ref. [15], the name *variable geometry active suspension* is introduced, and in Ref. [16], it is noted that there still is a fundamental lack of knowledge about this type of systems: “...all matters of detailed design are open, so that much research and development effort is needed to get the best out of the principle.”

The first results with the Delft active suspension were presented in the period 1989–1995. However, at present, there are still no vehicle manufacturers that have embraced the system. This fact can be contributed to a few negative aspects of the original concept. First, the design has major packaging issues. This is a result of the large space needed for the moving preloaded spring, the high number of moving parts, and the overall complexity of the system. Second, the actuator stiffness is a nonlinear function of the spring position. This might be a source of discomfort to the driver and even lead to instability in the absence of a secondary spring. Finally, the most important issue: safety and production cost. In most vehicles, the suspension is a safety critical component. Consequently, it should either never fail or there should be a suitable failsafe scenario. For the Delft active suspension, this would result in a backup electric motor, doubling the cost (and mass) of the total system. As our research focuses on secondary vehicle suspensions, this issue is less critical. Therefore, this topic will not be further addressed in this paper but it remains an open question how to ensure good failsafe behavior.

In Ref. [17], a modified fixed spring design with optimized geometry, called *electromechanical low-power active suspension (eLPAS)*, is presented that is expected to overcome the other negative aspects of the Delft active suspension design. The moving mass is reduced, which should further increase the overall performance. The packaging and stiffness issues are overcome by the chosen geometry.

Some first results, based on a design without the optimized stiffness, have been presented in Refs. [18,19]. In Ref. [18], the power consumption of the variable geometry actuator is evaluated in a quarter car suspension setting under idealized conditions (no friction or inertia effects). By means of a simulation study, the variable geometry actuator is shown to have a considerably lower peak power consumption than other systems (electric and hydraulic active suspension systems) without sacrificing any performance. In Ref. [19], the power consumption of the actuator is evaluated under nonideal conditions and it is shown that inertia (motor resistance) and friction play an important role.

Furthermore, in Ref. [20], the effectiveness of a variable geometry active suspension for commercial vehicles is investigated, especially focusing on the secondary suspension. The optimal vertical cabin control strategy is derived under idealized conditions, and the great performance potential with respect to driver comfort

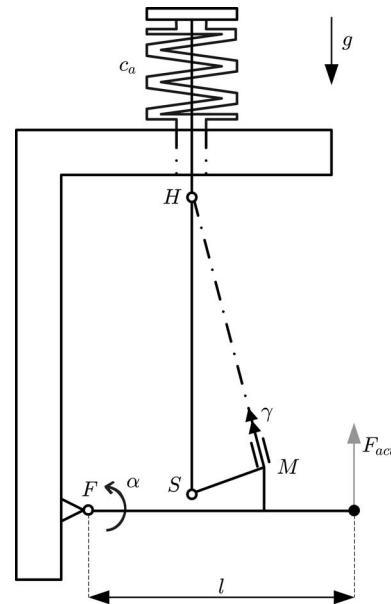


Fig. 2 Variable geometry actuator, eLPAS design

and energy requirements is demonstrated. However, the practical feasibility of the eLPAS design and the validity of the used eLPAS models is still an open question.

In this paper, the practical feasibility of the eLPAS design-variable geometry actuator, as described in Ref. [17], is evaluated. An actuator model is presented that includes the electric motor and friction characteristics. Using this model, a cascaded controller is designed and the steady-state and dynamic properties are evaluated on an experimental setup. Apart from the benefits of the designed stiffness and enhanced packaging options, a relatively high closed-loop bandwidth is obtained in comparison to previous designs [13]. It is concluded that the eLPAS design is feasible and that the model gives a fairly accurate representation of both the steady-state and dynamic prototype characteristics.

This paper is structured as follows: First, the eLPAS design is described and modeled. The model is used in Sec. 4 for the design of a cascaded control strategy, similar to that of Ref. [19]. It is shown using simulations that the energy characteristics for the new eLPAS design resemble those of the design used in Ref. [19]. The main contribution of this paper can be found in Sec. 5, where the practical feasibility of the design is evaluated by means of prototype tests and where the model and controller are validated.

## 2 eLPAS Design

The eLPAS design, as described in Ref. [17], is depicted in Fig. 2. It consists of a wishbone with length  $l$  that is connected to a frame using a joint  $F$ , which allows a rotation  $\alpha$ . Attached to the wishbone is an electric motor  $M$ , which driven direction ( $\gamma$ ) is perpendicular to the arm  $MS$ . The arm  $MS$  is connected to the rod  $HS$  through a ball joint  $S$ . In turn, the rod  $HS$  is connected to another rod through the rotational joint  $H$ , which allows rotation around two axes. This second rod is connected to a plate that constrains a spring with stiffness  $c_a$  and precompression  $F_s^0$ . The force within this spring gives rise to a force  $F_{act}$  at the end of the wishbone. This is the actuator force that varies for different values of  $\alpha$  and  $\gamma$  and needs to support the suspended mass.

The actuator is specifically designed for power efficiency. When the wishbone is horizontal ( $\alpha=0$ ), a fictitious cone is created with height  $HM$  and radius  $MS$ , similar to that obtained by the Delft active suspension [13]. Consequently, the arm  $HM$  can be rotated over any angle  $\gamma$  without changing the spring elongation. Ideally, for  $\alpha=0$ , in the absence of friction and inertia ef-

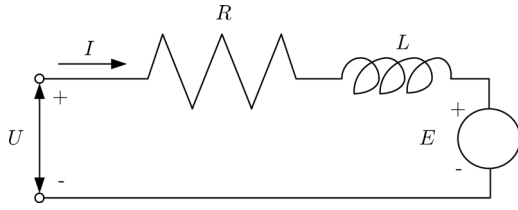


Fig. 3 Electrical scheme of a dc drive

fects, any rotation  $\gamma$  (and thus any actuator force  $F_{\text{act}}$ ) can be achieved without power usage. For any  $\alpha \neq 0$ , a disturbance moment ( $M_d$ ), induced by the spring force, acts on the electric motor ( $M$ ), which needs to be compensated to maintain a certain angle  $\gamma$ .

With respect to the string design as studied in Refs. [18,19], two major differences are visible. First of all, the string with length  $l_s$  is replaced by the two rods and rotational joint for durability reasons. Second, the orientation and positioning of the rotational axis of the electric motor (and gearbox) is changed to optimize the actuator stiffness characteristics.

For the derivation of the equations of motion, the reader is referred to Ref. [21].

### 3 Simulation Model

In this section, the components of the simulation model are discussed. These are used for the controller design later on.

**3.1 eLPAS—Variable Geometry Actuator Model.** The analytical model derived in Ref. [21] only holds when the frame (point  $F$ ) does not rotate with respect to the inertial frame at point  $O$ . This is in vehicle implementations not always the case. To overcome this limitation, a simulation model has also been created using *MATLAB SIMMECHANICS*, the multibody toolbox of *MATLAB SIMULINK*. The choice for *SIMMECHANICS* is mainly based on the good interface with *MATLAB SIMULINK* and the fact that it is relatively easy to use.

A comparison between the *SIMMECHANICS* implementation and the analytical model showed a nearly perfect match under steady-state conditions. The small differences that are present are mainly due to the more precise implementation of the masses of the rods in the *SIMMECHANICS* model.

**3.2 Electric Motor Model.** The eLPAS actuator angle is controlled by a three phase brushless permanent magnet (PM) dc motor in combination with a reductor and a powerful (42 V, 80 A) amplifier. The motor bandwidth is significantly higher than that of the total actuator assembly. For that reason, it might be warranted to assume exact tracking of any reference torque ( $T_r = T_r^{\text{ref}}$ ). However, a motor model is needed to gain insight in the power consumption of the actuator. Furthermore, under extreme circumstances, saturation of current and/or voltage may occur.

The brushless PM dc motor is typically characterized as having a trapezoidal back electromotive force (EMF) driven by rectangular pulse currents. As this mimics the operation of a brush PM dc motor, the name “brushless dc” fits even though it is in fact a synchronous ac motor ([22], Chap. 1).

The brushless PM dc motor differs from the brush PM dc motor in that the brushes needed for generating a varying magnetic field have been replaced by an electrical commutation (inverter). Moreover, where the brush PM dc motor has its permanent magnets in the stator and the varying magnetic field is realized in the rotor, it is the other way around in a brushless PM dc motor. As a result, the brushless PM dc motor is a nonlinear machine that is considerably more complex than the brush PM dc motor. Despite these differences, it is assumed that the equivalent electrical scheme of a brush PM dc motor, given in Fig. 3, also holds for the brushless

PM dc motor.

In practice, the three phase brushless PM dc motor is described by three of these electrical schemes, resulting in a maximum realizable torque that is roughly a factor 3/2 higher than that of a brush PM dc motor ([22], Sec. 8.3). Consequently, an error is introduced by this simplification. Still, the model will suffice to get a reasonable indication of the power requirements. For more reliable and detailed models, the reader is referred to, for example, in Ref. [23].

Adopting the electrical circuit depicted in Fig. 3, the motor dynamics is modeled as

$$L \frac{dI}{dt} = U - E - RI \quad (1)$$

where the back electromotive force voltage is given by

$$E = K_E \omega_m \quad (2)$$

$K_E$  is a motor constant,  $\omega_m$  is the rotational velocity of the motor,  $I$  is the current,  $U$  is the command voltage,  $L$  is the motor inductance, and  $R$  is the motor resistance. Furthermore, the effective actuation torque is given by

$$T_r = (T_{\text{rel}} - M_{\text{fric}})N \quad (3)$$

where  $N$  is the gearbox (reductor) ratio

$$T_{\text{rel}} = K_T I \quad (4)$$

$K_T$  is a motor constant, and  $M_{\text{fric}}$  is the friction moment of the motor and gearbox, which has to be incorporated in the model as it is an important source of energy dissipation [19].

**3.3 Friction Model.** As friction is expected to be one of the main effects of energy dissipation, it is important to obtain an accurate friction model. There is a vast amount of literature on friction modeling, see for example the survey given in Ref. [24]. The friction moment is modeled using a *LuGre* model [25] and is given by

$$M_{\text{fric}} = s_0 z + s_1 \dot{z} + s_2 \omega_m \quad (5)$$

with  $s_0, s_1, s_2$  as the friction parameters. Furthermore,  $z$  can be seen as the deflection of tiny bristles in the contact patch and

$$\dot{z} = \omega_m - \frac{|\omega_m|}{\beta} z \quad (6)$$

Moreover,

$$\beta = \frac{\{F_c + (F_s - F_c)e^{-(\omega_m/\omega_s)^2}\}}{s_0} \quad (7)$$

where  $F_c, F_s$ , and  $\omega_s$  are the parameters that determine the steady-state friction characteristic.

**3.4 Actuator Limitations.** In practice, the dynamic behavior of the electric motor will be limited due to the maximum voltage, the maximum current, and the danger of thermal overloading, which could damage the motor. Although important, the thermal behavior is not further evaluated in this paper given its complexity. The effect of the current and voltage limitations can be visualized by looking at the maximum size of a sine-shaped reference that can be followed, without saturation. The reference is given by

**Table 1 Friction and motor parameters**

Friction parameters		
	Value	Unit
$s_0$	15	N m
$s_1$	0.1	N m s
$s_2$	0.0042	N m s
$F_c$	0.2	N m
$F_s$	0.555	N m
$\omega_s$	11.8	rad/s
Motor parameters		
	Value	Unit
$K_E$	0.095	V s/rad
$K_T$	0.095	N m/A
$R$	0.13	$\Omega$
$L$	$2.5 \times 10^{-4}$	H
$N$	-59	-
$J_r$	0.70	kg m <sup>2</sup>
$I_{\max}$	75	A
$U_{\max}$	42	V

$$\gamma_{\text{ref}} = A \sin(2\pi ft) \quad (8)$$

The reference and its derivatives are constrained as

$$|\gamma_{\text{ref}}| \leq \gamma_{\max}$$

$$|\dot{\gamma}_{\text{ref}}| \leq \frac{\omega_m^{\max}}{N} = \frac{U_{\max}}{K_E N} \quad (9)$$

$$|\ddot{\gamma}_{\text{ref}}| \leq \frac{T_{\max} - |M_d|}{J} = \frac{N(K_T I_{\max} - |M_{\text{fric}}|) - |M_d|}{J}$$

by the physical limitations of the actuator with electric motor. Herein,  $M_d$  is the disturbance moment caused by the spring pretension for  $\alpha \neq 0$ . As a result, the actuator's working range is intrinsically limited by three constraints.

Consider the parameters as given in Table 1 and  $\gamma_{\max} = 90$  deg. The working range of the actuator under these conditions with  $M_{\text{fric}} = 0$  and  $\alpha = 0$  is represented in Fig. 4 by the area beneath the solid line. Furthermore, the three constraints are given by the dashed lines.

The first constraint, given by the horizontal line, can be increased by increasing  $\gamma_{\max}$ . However, raising it above 90 deg will have no beneficial effect on the maximum actuator force. The second constraint, given by the dashed line with -1 slope, is determined by the maximum rotational velocity of the electric mo-

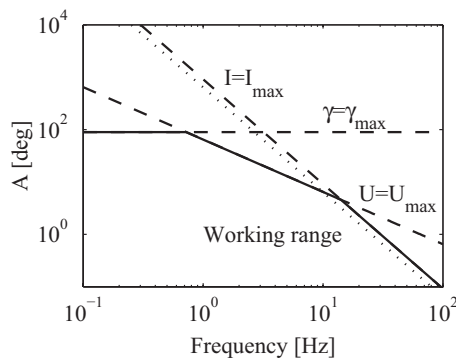


**Fig. 4 Actuator working range (under the solid line). Constraints for  $\alpha=0$  and  $M_{\text{fric}}^{\max}=0$  (dashed) and third constraint for  $M_{\text{fric}}^{\max}=0.9$  N m,  $\alpha=15$  deg (dotted).**

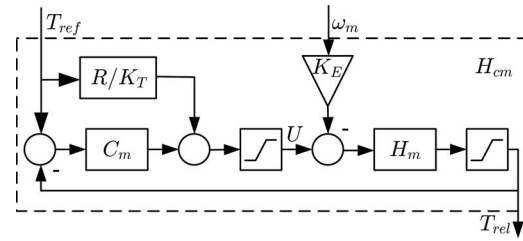


**Fig. 5 Block-scheme of the motor control loop**

tor. It can be increased by increasing the maximum voltage  $U_{\max}$ . The third constraint, given by the dashed line with -2 slope, is determined by the maximum rotational acceleration of the electric motor. It can be increased by increasing the maximum current  $I_{\max}$ .

In reality, the friction will be nonzero and also typically, there will be some rotation of the wishbone  $|\alpha| > 0$ . These two conditions will give rise to a shift of the third constraint. For the prototype, the maximum friction moment for high rotational velocities is approximately 0.9 N m. This is in accordance with the experimental data that will be shown later on. When applying this friction moment and a maximum disturbance moment (for  $\alpha = 15$  deg at  $\gamma=0$ ), the worst-case working range limitation can be approximated. This approximation is given in Fig. 4 by the dotted line.

## 4 Controller Design

A cascaded control strategy is chosen to control the actuator, similar to that given in Ref. [19]. As such, there is a motor controller, angle controller, and force controller. This strategy is chosen as it gives the possibility to constrain the reference angle  $\gamma_{\text{ref}}$  to the range of  $[-90$  to  $90]$  deg. As a result, it is possible to use linear techniques to generate the reference angle as a function of the reference force and actual force. The three controller modules are shortly discussed in Secs. 4.1–4.4.

**4.1 Electric Motor Control.** The inner most control loop is that of the torque controller, see Fig. 5. It consists of a standard PI-controller (Proportional Integral) with antiwindup,

$$C_m(s) = P_m + \frac{I_m}{s} \Big|_{I_m^{\max}} \quad (10)$$

and a resistance feedforward,

$$U_m^{\text{ff}}(s) = R I_{\text{ref}} \quad (11)$$

Herein,  $P_m$  and  $I_m$  are control gains and  $s$  is the Laplace variable. The transfer function  $H_m(s)$  between the realized motor torque  $T_{\text{rel}}$  and the effective voltage  $U - U_{\text{emf}}$  follows from Eq. (1),

$$H_m(s) = \frac{T_{\text{rel}}}{U - U_{\text{emf}}} = \frac{K_T}{Ls + R} \quad (12)$$

The controller brings the actual current close to the reference current and thus the realized torque  $T_{\text{rel}}$ , see Eqs. (3) and (4), close to the reference torque

$$T_{\text{ref}}(s) = K_T I_{\text{ref}} \quad (13)$$

Moreover, both the maximum voltage and current are constraint by the saturation blocks.

**4.2 Angle Control.** The second feedback loop is that of the angle controller, see Fig. 6. It consists of a lead-lag filter with integral action and antiwindup,



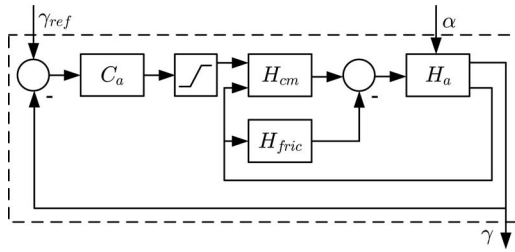


Fig. 6 Block-scheme of the angle control loop

$$C_a(s) = -P_a \left( \frac{s + D_a}{s + L_a} \right) - \frac{I_a}{s} \Bigg|_{f_a^{\max}} \quad (14)$$

The controller specifies a reference moment as a function of the tracking error between the reference angle and actual angle  $\gamma$ . The lead-lag filter is chosen as some additional damping is required to boost the obtainable bandwidth, while high frequency roll-off is needed to limit the influence of high frequency noise. Furthermore, the integrator is necessary to minimize the steady-state error. The control gain is negative as a result of the negative gear ratio  $N$ . The friction characteristic  $H_{\text{fric}}$  is defined by Eqs. (5)–(7) and the actuator hardware dynamics  $H_a$  follows from the SIMMECHANICS model.

**4.3 Force Control.** The upper control level consists of the force controller. Its task is to minimize the difference between the generated actuator force  $F_{\text{act}} = f(\gamma, \alpha)$  and the reference actuator force. In Ref. [19], this is done using a feedforward and feedback part. However, as an implementation is desired with a minimum number of sensors, it is assumed that the modeled  $F_{\text{act}} - \gamma - \alpha$  relation is exact and that the influence of  $J_w \ddot{\alpha}$  on the dynamics of the suspended mass is negligible. In practice, this assumption works out relatively well, as will be shown in Sec. 5.

By assuming that the modeled  $F_{\text{act}} - \gamma - \alpha$  relation is exact, the inverse relation  $\gamma_{\text{ref}} = f(F_{\text{act}}^{\text{ref}}, \alpha)$  can be used and the force feedback can be omitted. However, finding the inverse relation is quite difficult due to its complexity. Therefore, a 3D-lookup table, which specifies  $\gamma_{\text{ref}}$  for a given reference force  $F_{\text{ref}}$  and a measured deflection  $\alpha$ , seems preferable. Furthermore, as the effective stiffness can be designed such as is desirable, it is assumed that it does not need to be compensated. Consequently, a 2D-lookup table is used ( $F_{\text{act}} - \gamma$  relation for  $\alpha = 0$ ). Moreover, to limit the power consumption as a result of high frequency reference inputs, a 10 Hz first order low-pass filter is used to filter the reference force.

**4.4 Actuator Power Consumption.** In order to get an idea of the worst-case power consumption of the actuator, several simulations are performed. First, for  $\alpha = 0$ , several sine-shaped force references are tracked. Herein, the amplitude and frequency of the sines is varied. The maximum force amplitude for a certain frequency is obtained using Fig. 4. The results are given in Fig. 7.

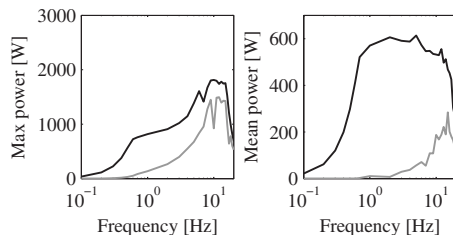


Fig. 7 Actuator worst-case power consumption. Mean (right) and maximum (left) power consumptions for  $\alpha = 0$ , when tracking sines of varying frequency and maximum amplitude  $A$ . Simulations with friction (black) and without friction (gray).

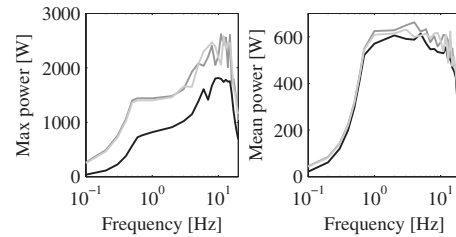


Fig. 8 Actuator worst-case power consumption. Mean (right) and maximum (left) power consumptions, when tracking sines of varying frequency and maximum amplitude  $A$ . Simulations with  $\alpha = -15$  deg (dark grey),  $\alpha = 0$  (black), and  $\alpha = 15$  deg (light grey).

It can be seen that the energy consumption of the eLPAS design is very low for low angular velocities ( $\dot{\gamma}$ ) but it increases for higher angular velocities. Consequently, high frequency reference signals result in a relatively large power consumption. Furthermore, it can be seen that friction affects account for the major part of the used power below 6 Hz. Above 6 Hz, the motor resistance starts to become important. The significant drop-off above 10 Hz is a result of the decreasing maximum velocities, resulting from the acceleration boundary, see Fig. 4. Furthermore, the 10 Hz low-pass filter in the force controller also reduces the maximum accelerations.

From simulations using the maximum force amplitude  $A_F$  and various fixed  $\alpha$ , it followed that the influence of the wishbone orientation  $\alpha$  on the mean power consumption under extreme circumstances is small, see Fig. 8 (right). However, the maximum power consumption varies significantly, see Fig. 8 (left), as a result of the spring force component that acts on the electric motor for  $\alpha \neq 0$ .

At this point, it is worth remarking that an active suspension with a peak power consumption of 2.5 kW has the potential to be very expensive from an energy perspective. Especially, considering the fact that a typical vehicle suspension requires four eLPAS actuators. In that case, the worst-case energy consumption will be similar to that of typical hydraulic solutions, see for example Ref. [26]. However, when tracking force references with half or one-fourth of the maximum amplitude, see Fig. 9, both the maximum and mean power consumptions drop significantly. This is very important to take into consideration when designing a global suspension controller.

Under normal working conditions, the reference force variations need to be kept as low as possible, without impairing the suspension performance (too much) [15]. Doing so, the energy requirements will remain far below the shown worst-case results. Overall, these simulations reinforce the notion that the eLPAS design has the potential to be relatively energy efficient.

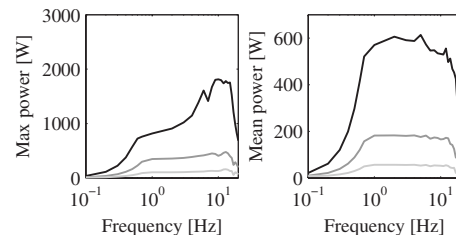
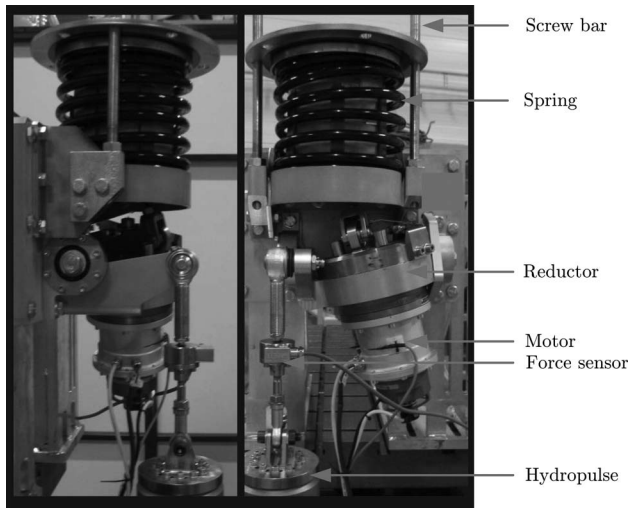


Fig. 9 Actuator mean (right) and maximum (left) power consumptions, when tracking sines of varying frequency for  $\alpha = 0$ . Simulations with  $A = A_{\text{max}}$  (black),  $A = A_{\text{max}}/2$  (dark gray), and  $A = A_{\text{max}}/4$  (light gray).



**Fig. 10 Experimental setup, front view (left) and side view (right)**

## 5 Experimental Validation

In this section, the steady-state and dynamic simulation results are compared with measurements obtained from an experimental setup. For the steady-state case, the results are evaluated for both of the models discussed in Sec. 3.1. The test-rig is discussed first.

**5.1 Prototype Setup.** The experimental setup is depicted in Fig. 10 for similar viewpoints as the model in Fig. 2. The two elements that dominate the picture are the electric motor with reductor on the one hand and the rather large spring on the other hand. The end of the wishbone is attached to a hydropulse, which is used to control the angle  $\alpha$ . The small block between the wishbone and the hydropulse is a force sensor. Furthermore, it can be seen that the rod  $HS$  (see Fig. 2) almost completely vanishes inside the spring.

The parameters of the experimental setup are given in Ref. [21]. Furthermore, the controller parameters are given in Table 2. These have been obtained using the SIMMECHANICS model. They are the result of tuning based on the sensitivity function, closed-loop bandwidth and step response overshoot. The bandwidth of the angle control loop is chosen relatively high (25 Hz) to reduce the friction effects on the tracking behavior. Using these parameters, the controller was also found to stabilize the experimental setup.

**5.2 Steady-State Validation.** For the steady-state analysis, a sine-shaped reference angle is used while  $\alpha=0$ . The frequency of the sine is chosen sufficiently low to minimize the influence of possible dynamic effects. The resulting actuator force measurements are compared with simulation results obtained with both the analytical model and the SIMMECHANICS model, see Fig. 11 (left).

A couple of things can be concluded from this figure. First of all, it can be seen that the SIMMECHANICS model and the analytical

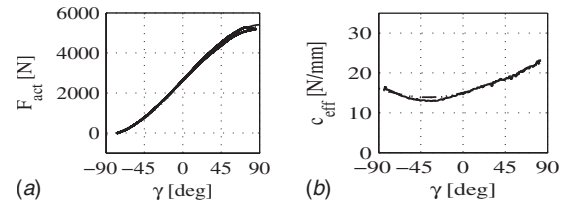


**Fig. 11 Actuator force (left) and effective stiffness (right) for  $\alpha=0$ : measurement (solid), analytic model (dash-dotted), and SIMMECHANICS model (dotted)**

model show very similar results. Furthermore, the difference between the models and the measurements is relatively small. However, for  $\gamma \rightarrow 90$  deg, there is a small hysteresis effect that is not included in the models. It may be a result of the bending of the wishbone due to the large spring force that acts at an increasing distance from the rotational joint. Changing the frequency of the sine-shaped reference from 0.01 Hz to 0.05 Hz did not change the magnitude of this effect.

The same reference signal is used for  $\alpha=-3.4$  deg and  $\alpha=4.2$  deg. The difference between these two force measurements is used to determine the effective stiffness around  $\alpha=0$ , see Fig. 11 (right). The effective stiffness for the models is determined in a similar way. It can be seen that the results almost show a perfect match. There is only a small difference around  $\gamma=-50$  deg. Furthermore, the effect of the relatively high spring stiffness is also clearly visible as the effective stiffness shows some variation as a function of  $\gamma$ . In retrospect, the steel spring may not have been the most ideal choice, as its characteristics also changed during the months of testing.

Using the measurements of the motor current from the same experiment as well as Eq. (4), it is possible to determine the actuation moment at the reductor  $M_r$ . However, this moment consists of both the friction moment and disturbance moment (Eq. (3)) so isolating the disturbance moment requires an additional computational step. Assuming that the friction moment is dominated by the coulomb friction for these low speeds, it can be given as

$$M_{\text{fric}}^* = \text{sign}(\omega_m) M_c \quad (15)$$

Herein, the coulomb friction is estimated to be  $M_c=0.5$  N m. Note that this is the moment at the motor so before the reductor. After the reductor, the influence is equal to 29.5 N m as a result of the gear ratio  $N$ . After subtraction of the estimated friction moment, the disturbance moment can be obtained. This moment, filtered with a 1 Hz second order zero-phase forward and reverse (causal and anticausal) filter, is given in Fig. 12.

It can again be seen that the difference between the analytical and SIMMECHANICS model is negligible. However, the difference between the models and the measurements is substantial. For  $\alpha=4.2$  deg, the results match quite well but for  $\alpha=0$  deg, it is clear that the measured disturbance moment is unequal to zero. This

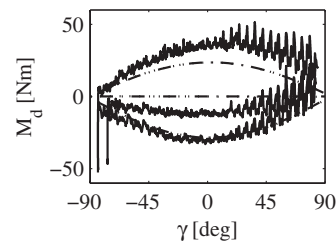


**Fig. 12 Actuator disturbance moment for  $\alpha=[-3.4, 0, 4.2]$  deg: measurement (solid), analytic model (dash-dotted), and SIMMECHANICS model (dotted)**

**Table 2 Controller parameters**

	Value	Unit
$P_m$	0.1	V/N m <sup>-1</sup>
$I_m$	50	V s/N m <sup>-1</sup>
$I_m^{\max}$	28	V
$D_a$	94.2	s <sup>-1</sup>
$P_a$	1500	N m
$I_a$	750	N m s
$I_a^{\max}$	2	N m
$L_a$	377	s <sup>-1</sup>

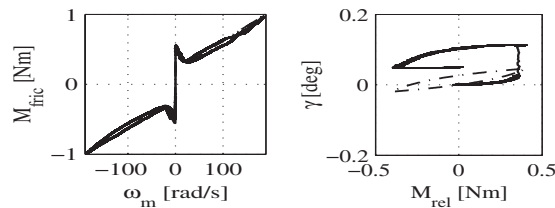


**Fig. 13 Friction characteristics measured (solid) and simulated (dash-dotted): friction moment as a function of the rotational velocity of the motor (left) and  $\gamma$  as a function of the realized motor moment in stiction**

might be a result of an alignment error of the hydropulse ( $\alpha_{\text{meas}} = 0 \neq \alpha$ ) or an indication that the constructed cone is not perfect. Moreover, the friction compensation might also introduce an error. The difference is largest for  $\alpha = -3.4$  deg. Furthermore, for all three  $\gamma$ -sweeps, a strange effect occurs for  $\gamma \rightarrow 90$  deg. This effect is probably also the result of the bending of the wishbone. Nevertheless, the size and shape of the modeled and measured disturbance moment as a function of  $\gamma$  and  $\alpha$  show a fair similarity. Furthermore, it should be noted that the maximum  $\alpha$  is larger than the values used in this test, i.e.,  $[-15, 15]$  deg.

**5.3 Dynamic Validation.** In this subsection, the SIMMECHANICS model is compared with the measurement results under dynamic conditions. First, the friction model is evaluated. Next, the closed-loop model is evaluated using a step-shaped reference. Finally, the transfer functions  $|F_{\text{act}}/F_{\text{ref}}|$  and  $|F_{\text{act}}/(I \sin \alpha)|$  are evaluated.

**5.3.1 Friction Model.** The friction modeling is evaluated with two experiments, inspired by Ref. [25]. In the first test, the friction-velocity characteristic is determined, and in the second test, the friction stiffness is evaluated.

For the first test, the connection rod *HS* (see Fig. 2) has to be disconnected and the bump-stops, which limit  $\gamma$ , need to be removed. Otherwise, the normal operating range,  $\gamma \in [-90, 90]$  deg, will be too small to accurately determine the friction moment given the relatively high acceleration levels. Although the spring force acting on the electric motor may in practice influence the friction characteristic, this effect cannot be determined so easily. In this disconnected configuration, a triangular velocity reference is followed, which makes a full sweep ( $0 \rightarrow \omega_m^{\text{max}} \rightarrow \omega_m^{\text{min}} \rightarrow 0$ ) in 50 s. The same experiment is repeated in simulation with the simulation parameters as given in Table 1. The results are given in Fig. 13 (left). It can be seen that the simulation and experimental data match well.

In the second test, the rods are reconnected and an open-loop test is executed. In this case, a triangular reference moment is used (with a period of 50 s) to determine the friction stiffness. The maximum reference moment remains below the coulomb friction level. The results are shown in Fig. 13 (right). The difference between the measurement and the simulation is mainly caused by a slight amount of sliding around  $M_{\text{ref}} = 0.4$  N m in the experimental setup. Nevertheless, given the similarities in curvature between measurement and simulation, it is concluded that the friction stiffness (tunable with the parameter  $s_0$ ) is modeled sufficiently accurate.

**5.3.2 Step Response.** In order to check the time response behavior of the model and experimental setup, a number of step responses are measured. First, a small force step of  $\pm 100$  (N) is performed. The results are given in Fig. 14 for a positive step (left) and a negative step (right). The force reference and responses are given in the top plots, and the power consumption is given in the bottom plots.

From the top plots in Fig. 14, it can be seen that the responses

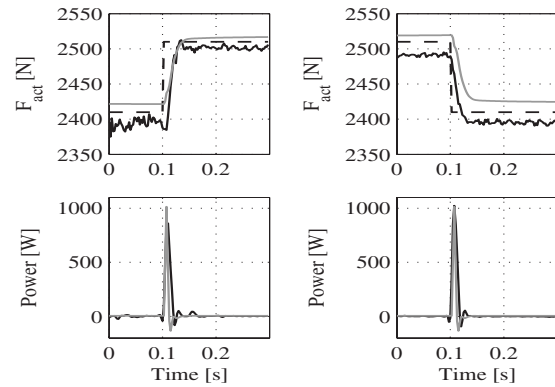


**Fig. 14 Small step: actuator force (top) and power consumption (bottom) for a positive step (left) and negative step (right). The lines represent the reference force (dashed), measurement (solid black), and simulation (grey).**

in simulation and experiment are quite similar when it comes to settling time and overshoot. However, there is a small constant offset. This is a result of the open-loop force control structure, small differences between the  $F_{\text{act}}-\gamma$  lookup table and the real actuator characteristics, friction, and sensor noise/drift. Furthermore, when looking at the power consumption (bottom plots), it is clear that the peak power consumption of the simulation and measurement are quite similar. However, the measured mean power consumption (33 W for both the positive and negative steps) is slightly higher than the simulated mean power consumption (18 W). Still, the differences are relatively small.

The differences increase for larger step responses, see Fig. 15. When evaluating the maximum size step responses, there is a large time period in which the maximum velocity is reached. This maximum velocity determines the slope of the  $F_{\text{act}}$  response in the top plots of Fig. 15. It can be seen that there is not much difference in maximum velocity, nor in the amount of overshoot between measurement and simulation. However, for the positive step (left), there is a difference in maximum acceleration visible. This might be caused by a difference in the amount of friction for  $\gamma = 90$  deg and  $\gamma = -90$  deg. Moreover, when looking at the power consumption (bottom plots), the difference between the two measurements is striking. This might be an indication that  $\alpha$  was not precisely zero during the test. Moreover, the simulated mean power consumption (367 W) is slightly higher than the measured

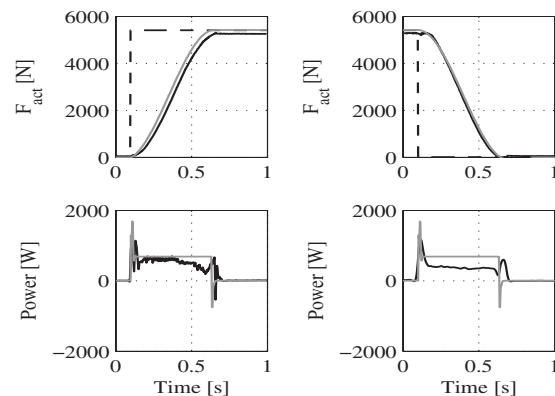


**Fig. 15 Maximum amplitude step: actuator force (top) and power consumption (bottom) for a positive step (left) and negative step (right). The lines represent the reference force (dashed), measurement (solid black), and simulation (grey).**



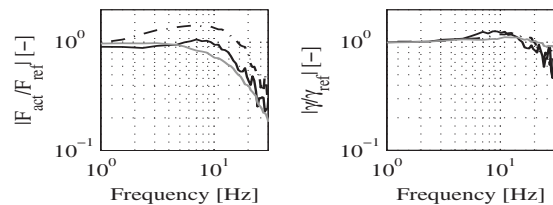


**Fig. 16** Transfer function estimate from  $F_{\text{ref}}$  to  $F_{\text{act}}$  (left) and  $\gamma_{\text{ref}}$  to  $\gamma$  (right) for  $\alpha=0$  and mean  $(\gamma)=0$ . Measurement with hydropulse (dash-dotted), measurement with hydropulse replaced by a fixed steel rod (solid black), and simulation (grey).

one (315 W for the positive and 255 W for the negative step). It can be seen that the main difference is located in the constant velocity part.

**5.3.3 Transfer Function Estimate.** To determine the closed-loop transfer function estimate, a zero mean Gaussian distributed (white noise) signal is used as force reference, filtered with a 15 Hz first order low-pass filter. First, the hydropulse is used to keep  $\alpha=0$ . However, the results using this approach show a large mismatch between measurement and simulation for the force loop, see Fig. 16 (left). This is especially remarkable as the closed-loop transfer function from  $\gamma_{\text{ref}}$  to  $\gamma$  does not show this difference, see Fig. 16 (right). Note that the difference between the  $\gamma$ -loop and force loop is due to the 10 Hz first order low-pass filter.

The large difference (in force transfer) between simulation and measurement with hydropulse is most likely a result of a resonance in the transfer function from  $\alpha$  to  $F_{\text{act}}$  around 6 Hz (Fig. 17). Therefore, the hydropulse is replaced by a solid steel rod and the experiment is repeated (solid line). Clearly, the measurement and simulation results match much better this way.

**5.3.4 Dynamic Stiffness.** The final topic of interest is the influence of  $\alpha$  on the actuator force. A filtered white noise reference is used for  $\alpha_{\text{ref}}$ , and the transfer function from  $l \sin \alpha$  to  $F_{\text{act}}$  is studied, see Fig. 17 (left). The horizontal line represents the design stiffness. Clearly, both the model and the experimental setup follow this stiffness for low frequent disturbances. However, there is an antiresonance at 6 Hz followed by a strong increase of the transfer function magnitude for higher frequencies as a result of the inertia of the wishbone in combination with the spring stiffness. Overall, it can be seen that there is a small offset between measurement and simulation as a result of the difference in the effective stiffness. Furthermore, the resonance seems to be damped more in the actual system than in simulation.

Instead of controlling the angle  $\gamma=0$ , it is also possible to demand that  $F_{\text{ref}}=F_{\text{act}}(0,0)=2555$  (N) while the hydropulse disturbs the system with filtered white noise. This can be seen as a “flying-carpet” controller, i.e., all “road” disturbances are suppressed without considering suspension travel or energy consumption. So, the actuator is controlled such that the force resulting from the effective eLPAS stiffness at various  $\alpha$  is compensated. The result is given in Fig. 17 (right). From this figure, it can be concluded that the influence of all disturbances below 8 Hz can be

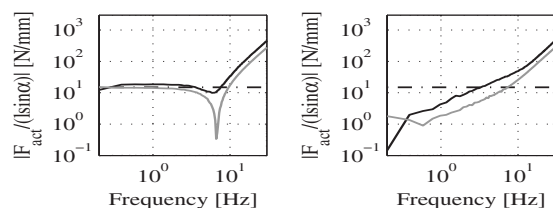


**Fig. 17** Transfer function estimate, measured (solid black) and simulated (grey), from  $l \sin \alpha$  to  $F_{\text{act}}$  for  $\gamma=0$  (left) and  $F_{\text{ref}}=0$  (right).

reduced significantly in simulation. On the actual setup, this boundary lies around 3 Hz. This difference is most likely a combination of uncompensated variations in the effective stiffness characteristic and inaccuracies in the force measurement.

## 6 Conclusions and Future Work

A model and a cascaded control strategy are presented for the eLPAS system. Friction and energy characteristics are included in the model, and their effect on the actuator’s dynamic working range has been evaluated. Using simulations, it has been shown that friction effects dominate the mean power consumption under worst-case conditions. The eLPAS design is very energy efficient for slow actuator force variations. Furthermore, when tracking a sine with a certain amplitude, the mean energy consumption will drop with more than 50% if the amplitude is reduced by a factor two.

The design is evaluated under steady-state and dynamic conditions on an experimental setup. Under steady-state conditions, the results show a good match between simulations and measurements. Under dynamic conditions, the results vary. Overall, the force and angle characteristics are modeled reasonably well. The visible differences can, in general, also be contributed to the testing conditions. Concerning the energy consumption, the model seems to be less accurate. Still, the results show a qualitative match.

Due to the intrinsic nonlinearities in the system, it is difficult to fully demonstrate the predictive quality of the presented models. Still, all our observations indicate that the eLPAS design is feasible and that the model gives a fairly accurate representation of both the steady-state and dynamic prototype characteristics. In the future, this model will be embedded in vehicle models for the purpose of controller development and further evaluation of the effectiveness of the eLPAS system.

## Acknowledgment

The authors would like to thank the TNO team that assisted with the development of the experimental setup.

## References

- [1] Muijterman, J. H. E. A., 1997, “Flexible Objective Controllers for Semi-Active Suspensions With Preview,” Ph.D. thesis, Eindhoven University of Technology, Eindhoven, The Netherlands.
- [2] Hrovat, D., 1997, “Survey of Advanced Suspension Developments and Related Optimal Control Applications,” *Automatica*, **33**(10), pp. 1781–1817.
- [3] Han, S. S., Choi, S. B., Park, J. S., Kim, J. H., and Choi, H. J., 2003, “Robust Sliding Mode Control of an Electrorheological Suspension System With Parameter Perturbations,” *Int. J. Veh. Des.*, **33**(1/2/3), pp. 279–295.
- [4] Fischer, D., and Isermann, R., 2004, “Mechatronic Semi-Active and Active Vehicle Suspensions,” *Control Eng. Pract.*, **12**, pp. 1353–1367.
- [5] Ballo, I., 2001, “Properties of Air Spring as a Force Generator in Active Vibration Control Systems,” *Veh. Syst. Dyn.*, **35**(1), pp. 67–72.
- [6] Soliman, A. M. A., and Crolla, D. A., 2001, “Limited Bandwidth Active Suspension Employing Wheel Base Preview,” *SAE World Congress*, Paper No. 2001-01-1063.
- [7] Alleyne, A., and Liu, R., 2000, “A Simplified Approach to Force Control for Electro-Hydraulic Systems,” *Control Eng. Pract.*, **8**, pp. 1347–1356.
- [8] HeiBing, B., and Ersoy, M., 2007, *Fahrwerkhandbuch*, Friedrich Vieweg & Sohn Verlag, Wiesbaden pp. 533–536.
- [9] Encicà, L., 2008, “Space-Mapping Optimization Applied to the Design of a Novel Electromagnetic Actuator for Active Suspension,” Ph.D. thesis, Eindhoven University of Technology, Eindhoven, The Netherlands.
- [10] 2007, <http://www.bose.com/suspension>
- [11] Nakano, K., and Suda, Y., 2004, “Combined Type Self-Powered Active Vibration Control of Truck Cabins,” *Veh. Syst. Dyn.*, **41**(6), pp. 449–473.
- [12] van der Knaap, A. C. M., 1989, “Design of a Low Power Anti-Roll/Pitch System for a Passenger Car,” MS thesis, Delft University of Technology.
- [13] Venhovens, P. J. Th., and van der Knaap, A. C. M., 1995, “Delft Active Suspension (DAS). Background Theory and Physical Realization,” *Smart Vehicles*, J. P. Pauwelussen and H. B. Pacejka, eds., Taylor & Francis, London, pp. 139–165.
- [14] van der Knaap, A. C. M., Venhovens, P. J. Th., and Pacejka, H. B., 1994, “Evaluation and Practical Implementation of a Low Power Attitude and Vibration Control System,” *International Symposium on Advanced Vehicle Control (AVEC)*.
- [15] Sharp, R. S., 1998, “Variable Geometry Active Suspension for Cars,” *Comput. Control Eng. J.*, **9**(5), pp. 217–222.



- [16] Watanabe, Y., and Sharp, R. S., 1999, "Mechanical and Control Design of a Variable Geometry Active Suspension System," *Veh. Syst. Dyn.*, **32**, pp. 217–235.
- [17] van der Knaap, A. C. M., Teerhuis, A. P., Tinsel, R. B. G., and Verschuren, R. M. A. F., 2008, "Active Suspension Assembly for a Vehicle," International Patent No. WO 2008/049845.
- [18] Evers, W.-J., Besselink, I. J. M., van der Knaap, A. C. M., and Nijmeijer, H., 2008, "Analysis of a Variable Geometry Active Suspension," International Symposium on Advanced Vehicle Control, pp. 350–355.
- [19] Evers, W.-J., Besselink, I. J. M., van der Knaap, A. C. M., and Nijmeijer, H., 2008, "Modeling, Analysis and Control of a Variable Geometry Actuator," IEEE Intelligent Vehicles Symposium, pp. 251–256.
- [20] Evers, W.-J., Besselink, I. J. M., Teerhuis, A. P., and Nijmeijer, H., 2010, "On the Achievable Performance Using Variable Geometry Active Secondary Suspension Systems in Commercial Vehicles," *Veh. Syst. Dyn.*, accepted for publication.
- [21] Evers, W.-J., 2010, "Improving Driver Comfort in Commercial Vehicles: Modeling and Control of a Low-Power Active Cabin Suspension System," Ph.D. thesis, Eindhoven University of Technology, Eindhoven, The Netherlands.
- [22] Hanselman, D. C., 2003, *Brushless Permanent Magnet Motor Design*, 2nd ed., Writers' Collective, Cranston, RI.
- [23] Lomonova, E. A., 1997, *A System Look at Electromechanical Actuation for Primary Flight Control*, Vol. 3(2), Delft University Press.
- [24] Armstrong-Hélouvry, B., Dupont, P., and Canudas De Wit, C., 1994, "A Survey of Models, Analysis Tools and Compensation Methods for the Control of Machines With Friction," *Automatica*, **30**(7), pp. 1083–1138.
- [25] Canudas De Wit, C., Olsson, K., Aström, K. J., and Lischinsky, P., 1995, "A New Model for Control of Systems With Friction," *IEEE Trans. Autom. Control*, **40**(3), pp. 419–425.
- [26] Uffelman, F., and Wiesmeijer, A., 1992, "Active Cab Suspension for Trucks: Technical Realization and Achievable Ride Comfort," 24th FISITA Congress, London, England, pp 75–85.